Double functionality concurrent dual–band self–oscillating mixer

Mabel Pontón, *Member, IEEE*, Amparo Herrera, and Almudena Suárez, *Fellow, IEEE*

Abstract—A concurrent dual–band self–oscillating mixer (SOM), based on a ring-shaped stepped-impedance resonator, is proposed and analyzed in detail. Taking advantage of the ring even and odd resonances, the circuit can operate in concurrent dual quasi–periodic mode and injection–locked mode. In the second case, it behaves as a dual-band zero–IF mixer. Initially an analytical study of the SOM behaviour in the two modes is presented. Then a variety of accurate numerical methods are used for an in-depth investigation of the main aspects of its performance, including stability, conversion gain, linearity, and phase noise. The recently proposed contour-intersection technique and the outer-tier perturbation analysis are suitably adapted to the SOM case. A method is also presented to distinguish the parameter intervals leading to heterodyne and to zero-IF operation at both the lower and upper frequency bands. In the zero-IF SOM, the possible instantaneous unlocking in the presence of modulated input signals is investigated and avoided. The methods have been applied to a dual mixer at the frequencies 2.4 GHz and 4.1 GHz.

Index Terms— harmonic balance, oscillators, phase-noise analysis, stability analysis.

I. INTRODUCTION

The recent works [1]-[3] present a novel concept to obtain zero-IF frequency conversion using an injection-locked oscillator, suitably designed and biased to enhance its mixing capabilities. The so-called zero-IF self-oscillating mixer (SOM) enables the implementation of compact transmitters and receivers. The concept is of general interest in systems requiring a small size and weight, such as the μRFID tag proposed in [1]. Considering also the increasing demand of multiband wireless systems, the work [4] proposed a concurrent dual-band zero-IF SOM, which extends the compact frequency conversion to simultaneous operation in two frequency bands. This requires a concurrent dual-frequency oscillator at two incommensurable fundamental frequencies ω_1 and ω_2 [5]-[7], which corresponds to a doubly autonomous quasi–periodic solution. In the concurrent dual-frequency zero-IF SOM, each oscillation gets locked to its corresponding RF signal [4], so the circuit behaves as a concurrent dual-frequency injection-locked oscillator. A major challenge in the design of concurrent dual-frequency oscillators is the robustness of this concurrent operation mode [8], which mathematically coexists with two periodic solutions, at ω_1 and ω_2, respectively, and with the DC solution. For a reliable concurrent operation, the quasi–periodic solution at ω_1 and ω_2 must be the only stable one.

Recently, a concurrent dual-frequency oscillator based on a stepped-impedance loop resonator [9]-[11] has been proposed [12]-[14]. This element enables a compact implementation of two orthogonal resonances at ω_1 and ω_2 [1]with high quality factor and an excellent isolation. It has the advantage of a compact size, usually much smaller than the one resulting from two independent resonators with similar quality factors. With this element, low phase noise can be achieved, as shown in [15], where a ring-shaped step-impedance resonator was used to reduce the phase-noise spectral density of a single-frequency voltage-controlled oscillator (VCO).

Departing from a dual-frequency oscillator based on a ring-shaped resonator, the work [4] presented a double functionality SOM, able to operate both as a zero-IF SOM and as a heterodyne SOM [16]-[18]. In heterodyne mode each of the two concurrent oscillations (ω_1 and ω_2) mixes with its corresponding input signal, that is, ω_{in1} mixes ω_1 and ω_{in2} mixes with ω_2, to provide two distinct intermediate-frequency (IF) outputs. This work expands [4] with a nonlinear analysis of the SOM in both heterodyne and zero-IF modes. Initially, an analytical investigation of the SOM behavior in the two modes is presented. It provides insight into the conversion gain, linearity, and oscillation extinction, in the heterodyne case, and the injection-locked operation and mechanisms for the amplitude and frequency demodulation, in the zero IF case. Then, the transistor-based dual-band SOM is addressed with a variety of numerical methods based on harmonic balance (HB).

The first goal will be the detailed a stability analysis of the ring-resonator dual-frequency oscillator, considering the DC solution, the distinct periodic oscillations at ω_1 and ω_2, and the concurrent quasi-periodic oscillation at ω_1 and ω_2. In heterodyne mode, the SOM will be analyzed through an extension of the contour-intersection method proposed in [19]-[20] to quasi-periodic regime. The variation of the conversion gain is analyzed exporting a gain surface that must be interpolated at the solution points obtained through the contour intersection. The phase noise is analyzed with a perturbation formulation based on an outer-tier admittance-type description of the SOM circuit. The input-generator values (in terms of frequency and power) for operation as a heterodyne SOM and as zero-IF SOM are distinguished through a bifurcation analysis [21]-[25]. In particular, one must obtain the loci at which the self-oscillation is extinguished (Hopf locus) [21]-[25] and the locus at which this oscillation is locked to the input source (turning-point

locus) [26]. In zero-IF mode, it will be relevant to know the minimum input power required for the oscillation locking at each input frequency. This is because under insufficient input power, there can be instantaneous unlocking phenomena during the modulation period.

The methods have been applied to a dual-band SOM at 2.4 GHz and 4.1 GHz. The prototype demonstrates the possibility to implement a compact dual-frequency converter, though no attempt has been made to obtain a fully optimized design. Instead, the focus is placed on the development of analysis tools to optimize its performance in future implementations.

The paper is organized as follows. Section II presents an approximate analytical model that provides qualitative insight into the SOM behavior. Section III addresses the design of the concurrent dual-band SOM and its stability analysis. Section IV describes the behavior of the heterodyne SOM. Section V presents the analysis of the zero-IF SOM.

II. APPROXIMATE ANALYTICAL MODEL OF A SOM

This section presents an approximate analytical model of the SOM, considering a single-band operation to avoid an excessive complexity. The circuit analyzed is shown in Fig. 1. The transistor is represented with a nonlinear current function [depending on the control voltage $v(t)$] and two capacitors C_1 and C_2. The oscillation is enabled by a series-feedback resonator with the impedance Z_S.
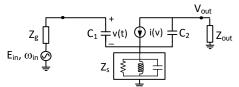

Fig. 1. Circuit considered in the approximate analytical study of the heterodyne and zero-IF SOM.

A. Heterodyne SOM

For simplicity, the SOM analysis will be limited to the oscillation frequency ω_o and the input frequency ω_{in}, so the control voltage $v(t)$ of the nonlinear current $i(v)$ is:

$$v(t) = V_o \cos(\omega_o t) + \text{Re}\left[V_1 e^{j(\omega_{in}t)}\right] \tag{1}$$

The phase of the (autonomous) oscillation component is arbitrarily set to zero and V_1 is a phasor since there must be a phase difference with respect to the input generator at ω_{in}. The nonlinear current is $i(v) = g_m v(t) + g_2 v^2(t) + g_3 v^3(t)$, where $g_m > 0$ and $g_3 < 0$. Applying Kirchoff's laws at ω_o and ω_{in}:

$$V_o + A_y(\omega_o)\left(g_m V_o + \frac{3}{4} g_3 V_o^3 + \frac{3}{2} g_3 |V_1|^2 V_o\right) = 0 \quad \text{(a)}$$

$$V_1 + A_y(\omega_{in})\left(g_m V_1 + \frac{3}{4} g_3 |V_1|^2 V_1 + \frac{3}{2} g_3 V_o^2 V_1\right) + \tag{2}$$

$$A_g(\omega_{in})E_{in} = 0 \quad \text{(b)}$$

where E_{in} is the input amplitude and $A_y(\omega), A_g(\omega)$ account for the passive linear elements. They are calculated with the transfer functions:

$$A_y(\omega) = -\frac{V(\omega)}{I}\bigg|_{E_{in}=0} \quad ; \quad A_g(\omega) = -\frac{V(\omega)}{E_{in}}\bigg|_{V=0} \tag{3}$$

where I is the current of the nonlinear source. In the absence of input power, $|V_1| = 0$, (2)(a) particularizes to the free-running oscillation at ω_o. In this simple model, the oscillation

frequency is obtained from $\text{Im}[A_y(\omega_o)] = 0$. The capacitances C_1 and C_2 will give rise to a small shift with respect to the resonance frequency of $Z_S(\omega)$. One should note that even when $E_{in} \neq 0$, system (2) admits a solution with zero oscillation amplitude $V_o = 0$, which should be unstable and avoided in the SOM analysis. In the numerical methods this will be done with the aid of an auxiliary generator (AG) [26].

When $E_{in} > 0$, $i(v)$ provides an additional term at the intermediate frequency $|\omega_{in}-\omega_o|$ that, in this simplified analysis, can be approached as $I_{IF} = g_2 V_o V_1$. With $Z_g = Z_{out} = R_o$, and assuming a small C_2, the conversion gain is approximated as:

$$G_{IF} = \frac{4(g_2 V_o)^2 |V_1|^2 R_o^2}{E_{in}^2} \tag{4}$$

For small E_{in}, one can neglect the second term in the nonlinear current of 2(b), which provides the small-signal gain:

$$G_{ss} = 4(g_2 V_o)^2 \frac{|A_g(\omega_{in})|^2 R_o^2}{\left|1 + A_y(\omega_{in})\left(g_m + \frac{3}{2} g_3 V_o^2\right)\right|^2} \tag{5}$$

The higher V_o, the smaller the second term in the denominator, due to the opposite signs of g_m and g_3. Thus, the small-signal gain increases with V_o, g_2 and the transfer function $|A_g|$.
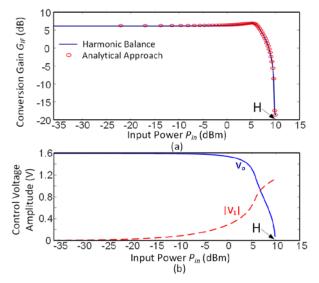

Fig. 2. Heterodyne SOM. Analytical model validated with HB simulations. (a) Conversion gain versus P_{in}. (b) Variation of V_o and $|V_1|$ versus P_{in}.

Now we will consider the variation of G_{IF} in (4) versus $P_{in} = E_{in}^2/(8R_o)$. This is shown in Fig. 2(a) where the results of system (2) have been validated with a harmonic-balance (HB) simulation of the circuit in Fig. 1, with the aid of an AG [8], [23]. Fig. 2(b) presents the corresponding variation of V_o and $|V_1|$. In agreement with (2)(a), when E_{in} increases, the larger $|V_1|$ leads to a reduction of V_o, due to the opposite signs of g_m and g_3. The analytical model also explains the gain expansion in Fig. 2(a). The relatively fast decrease of V_o may give rise to an increase in the slope of $|V_1|$ versus P_{in} [Fig. 2(b)] since the counteracting effect of $g_3 V_o^2 V_1 3/2$ in 2(b) becomes smaller when V_o decreases. Eventually, the gain decreases with V_o and tends to $-\infty$ when the oscillation is extinguished.

A relevant nonlinear effect in a SOM is the oscillation extinction when increasing P_{in}, which occurs at an inverse

Hopf bifurcation [21]-[25], denoted with H in Fig. 2, and obtained by setting $V_o = 0$ in (2)(a):

$$1 + A_y(\omega_o)\left(g_m + \frac{3}{2} g_3 |V_{1H}|^2\right) = 0 \qquad (6)$$

The corresponding P_{in} is calculated replacing $|V_{1H}|$ in (2)(b). For a same g_m, P_{in} at the Hopf bifurcation will be higher for a smaller $|g_3|$ and a larger detuning of ω_{in} from the original free-running frequency.

B. Zero-IF SOM

In the zero-IF SOM, the oscillator is injection locked to the input source at ω_{in}, which is the only fundamental frequency. The circuit behavior is described with the two following equations at DC and ω_{in}:

$$V_{DC} + A_y(0)\left(g_2 \frac{V_o^2}{2}\right) = 0 \qquad (a)$$

$$V_o + A_y(\omega_{in})\left(g_m V_o + \frac{3}{4}g_3 V_o^3\right) + A_g(\omega_{in})E_{in}e^{j\phi} = 0 \quad (b)$$

$$(7)$$

where for better insight some terms have been neglected. The phase origin is set at the control voltage, V_o, and ϕ is the opposite of the phase shift with respect to the input source. In our simplified model, (7)(b) can be solved independently of (7)(a). For each ω_{in}, it provides a system of two complex equations in V_o and ϕ. When also considering distinct values of E_{in}, one obtains a curve family versus ω. This is shown in Fig. 3(a), where the curves are traced in terms of the current through C_1. To understand the family, one should note that for $E_{in} = 0$, (7)(a) particularizes to the free-running oscillation point, ω_o, V_o, plus the trivial solution $V_o = 0$. For small E_{in}, a linearization about the free-running point, ω_o, V_o, gives rise to an ellipse and the trivial solution evolves into a low-amplitude curve of periodic solutions at ω_{in}. Thus, one obtains two isolated curves, though only the closed curve corresponds to injection-locked operation. As E_{in} increases the closed curve deviates from a perfect ellipse [$E_{in} = 0.2$ V in Fig. 3(a)]. The boundaries of the locking band are given by the two turning points of the closed curve, though only its upper or lower section is stable [23]-[24]. When further increasing E_{in}, the two curves merge into one that exhibits folding due to the presence of turning points [$E_{in} = 0.3$ V and $E_{in} = 0.4$ V in Fig. 3(a)].
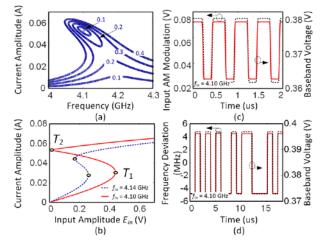

Fig. 3. Zero-IF SOM. (a) Family of solution curves versus ω_{in} for different E_{in} values. (b) Two solution curves traced versus E_{in}, each for a different ω_{in}. (c) Amplitude modulation. (b) Frequency modulation.

The turning points in the curves obtained for the lower E_{in} correspond to local-global bifurcations [21]-[23] at which an incommensurate oscillation arises with a zero value of the beat frequency. This beat frequency grows quickly when moving away from the turning points and agrees with the IF frequency in heterodyne mode. In fact, the merged curves of Fig. 3(a) are stable only in a certain frequency band about ω_o, delimited by Hopf bifurcations, at which an incommensurate oscillation arises from zero amplitude. The curves in Fig. 2(b) constitute an example of the generated quasi-periodic solutions, not traced in Fig. 3(a). In zero-IF mode, the frequency of the input source must belong to the stable locking bands, which are broader for higher P_{in} [Fig. 3(a)]. In heterodyne mode, one must avoid these bands. More details on the frequency selection are given in Section V.

One can also represent the injection locked curves versus E_{in} at constant ω_{in}, as done in Fig. 3(b), where two distinct ω_{in} values are considered. Roughly speaking, the low-amplitude section of these curves (from zero to the first turning point T_1) corresponds to solutions in which the self-oscillation is not excited. For low E_{in}, they are in the low-amplitude curves of Fig. 3(a), below the closed ones. In turn, the upper and middle sections correspond to the closed curves in Fig. 3(a). When increasing E_{in} from zero, the circuit is initially unlocked and exhibits a quasi-periodic solution [not represented in Fig. 3(b)]. It becomes locked at the turning point T_2. The E_{in} value at T_2 will be smaller for a smaller detuning with respect to the free-running frequency. A change of E_{in} at a constant ω_{in}, will give rise to a variation of V_o, and, in turn, to a variation of V_{DC}, as shown in (7)(a). Assuming an input amplitude modulation and neglecting initially any dynamic effects due to the modulation frequency, one will obtain a baseband signal, resulting from the time variation of the previous DC term. Under faster variations, one should consider time-varying variables $V_{DC}(t), V_o(t), \phi(t)$ at the scale of the modulation, so the frequency-dependent functions A_y and A_g will be expressed in a first-order Taylor series [28] about DC and ω_{in}. The multiplication by the frequency increment implies a time differentiation [29], so one obtains the envelope-domain system:

$$A_V(0)V_{DC}(t) - j\left.\frac{dA_V(\omega)}{d\omega}\right|_{\omega=0}\dot{V}_{DC}(t) + A_{yN}(0)\left(g_2\frac{V_o^2(t)}{2}\right)$$

$$-j\left.\frac{dA_{yN}(\omega)}{d\omega}\right|_{\omega=0} g_2 V_o(t)\dot{V}_o(t) = 0$$

$$A_V(\omega_{in})V_o(t) - j\left.\frac{dA_V(\omega)}{d\omega}\right|_{\omega=\omega_{in}}\dot{V}_o(t) + A_{yN}(\omega_{in})\left(g_m V_o(t) + \frac{3}{4}g_3 V_o^3(t)\right) -$$

$$j\left.\frac{dA_{yN}(\omega_o)}{d\omega}\right|_{\omega=\omega_{in}}\left(g_m + \frac{9}{4}g_3 V_o^2(t)\right)\dot{V}_o(t) + A_{gN}(\omega_o)E_{in}(t)e^{j\phi(t)} -$$

$$j\left.\frac{dA_{gN}(\omega_o)}{d\omega}\right|_{\omega=\omega_{in}}\left(\dot{E}_{in}(t)e^{j\phi(t)} + j\dot{\phi}(t)E_{in}(t)e^{j\phi(t)}\right) = 0$$

$$(8)$$

where A_y and A_g have been re-defined to avoid frequency-dependent denominators. Note it would be possible to consider higher order terms in the Taylor-series expansion. Fig. 3(c) presents the behavior under an input amplitude modulation with a rectangular waveform of 2 MHz and amplitude 0.05 V, at $f_{in} = 4.1$ GHz and $E_{in} = 0.025$ V. The injection-locked oscillator can also demodulate FM signals [30]-[31]. Under a change of ω_{in} in injection-locked conditions, there will be a variation of both ϕ and V_o, as

gathered from (7)(b). From (7)(a), the latter will give to a change in V_{DC}, so the circuit should be able to demodulate FM signals, as shown in Fig. 3(d), where an FSK modulation of 1 Mbps has been introduced at $f_{in} = 4.1$ GHz and $E_{in} = 0.1$ V. The sensitivity to the modulation will increase with the slope of the oscillation amplitude versus ω_{in}.

III. DESIGN AND STABILITY ANALYSIS OF THE CONCURRENT DUAL-FREQUENCY OSCILLATOR

A. Circuit topology

The circuit in Fig. 4(a)–(b) operates as a concurrent dual-band SOM, due to its capability to exhibit two simultaneous oscillations at the frequencies ω_1 and ω_2. Following [12], the circuit is based on a ring-shaped stepped-impedance resonator, which enables an implementation of two equivalent one-wavelength resonators in a single compact-size resonator. As in the single-frequency VCO of [15], two transistor devices are connected to two of the resonator ports. Our goal has been to obtain a demonstrator independent resonance modes at the incommensurate frequencies $f_1 = 2.4$ GHz and $f_2 = 4.1$ GHz; these values enable a comparison of the phase-noise spectral density with previous single-frequency realizations [32]-[33] using similar components. The resonator design departs from the structure sketched in Fig. 5(a), which contains four sections of $\pi/2$ electrical length at f_0. To achieve the two resonances at f_1 and f_2, the ratio R_Z between the characteristic impedances Z_2 (of the higher-impedance section) and Z_1 (of the lower-impedance section) must be:

$$R_Z = \tan^2\left(\frac{\theta_0 f_2}{f_0}\right) \tag{9}$$

where $\theta_0 = 2\pi/8$. In our case, ratio $R_Z = 2.32$. In these conditions, when exciting the resonator at the Port 1 (3) one obtains resonance frequency at $f_1 = 2.4$ GHz ($f_2 = 4.1$ GHz).
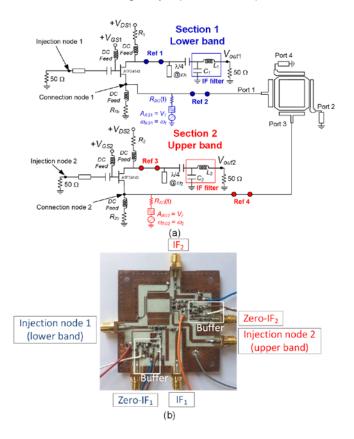

Fig. 4. Proposed dual–frequency self–oscillating mixer for operation in concurrent dual heterodyne mode and concurrent dual zero-IF mode. Prototype built on Rogers 4003C substrate. (a) Schematic. (b) Photograph.

The ring is introduced into the oscillator with the aid of coupled lines, like in [12]. After slightly optimizing the dimensions, the electromagnetic simulations provide the two independent resonances shown in Fig. 5(b) and Fig. 5(c), where the input susceptance has been represented versus frequency. The two unloaded quality factors are $Q_1 = 235$ at $f_1 = 2.4$ GHz and $Q_2 = 140$ at $f_2 = 4.1$ GHz.
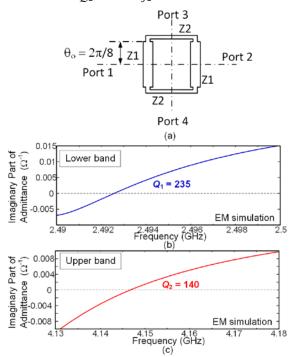

Fig. 5. Electromagnetic simulation of the stepped-impedance ring-shaped resonator. (a) Sketch of the original design to obtain two independent resonances at $f_1 = 2.4$ GHz and $f_2 = 4.1$ GHz. (b) Resonance at 2.4 GHz after inclusion of the coupled line sections (see resonator in Fig. 4). (c) Resonance at 4.1 GHz after inclusion of the coupled line sections.

Here, the two independent modes of the resonator are used to fulfill the oscillation conditions at ω_1 and ω_2, respectively. The ring resonator is connected to the source terminals of the two transistor devices as the only feedback element. The two circuit sections, denoted as Section 1 and Section 2 in Fig. 4(a), oscillate at the respective frequencies ω_1 (lower) and ω_2 (higher). The two RF input signals, at ω_{in1} and ω_{in2}, are introduced through a transmission-line section used for matching purposes. For heterodyne SOM operation, each sub-oscillator includes an open–circuited $\lambda/4$ stub (at ω_1 and ω_2, respectively) connected to the drain terminal [Fig. 4(a)], as well as a low–pass filter. Under zero-IF operation, if there is a negligible spectrum content near DC, the output signal can still be extracted through the same output network. It can also be extracted from the drain-bias network with the aid of a buffer. At each frequency the circuit combines the oscillator and mixer functions and can provide conversion gain. The total consumption in concurrent operation is 48 mW. As seen in Fig. 4(b), the stepped-impedance resonator is the largest circuit component. It has a footprint of 15 mm x 15 mm, whereas that of the packaged transistors is 2 mm x 2.1 mm.

Prior to the introduction of the RF signals, the circuit must exhibit two concurrent oscillations at the frequencies ω_1 and ω_2. For a reliable operation, this doubly-autonomous quasi-

periodic solution must be the only stable one. However, due to the circuit autonomy, this solution coexists with a DC solution and two distinct periodic solutions at ω_1 and ω_2, which must be unstable. In the following, a detailed stability analysis of the three types of solution is presented.

B. Stability of the DC solution

The stability analysis of the dual-band SOM in Fig. 4(a) through the pole-zero identification of a closed-loop transfer function [34]-[38] may suffer from insufficient observability, due to the high isolation between the two sub-oscillators. This identification relies on the fact that all the closed-loop transfer functions that can be defined in a linear system share the same denominator and therefore should exhibit the same poles [34]-[38], formally agreeing with the *roots* of the characteristic determinant that define the stability properties. Unlike the poles, the zeroes depend on the closed-loop transfer function, and cancellations/quasi–cancellations of poles and zeroes may take place in some of these functions [34]-[38]. If the cancelled/quasi-cancelled poles are in the right-hand side of the complex plane (RHS), one will miss instabilities. This is usually due to a low observability of some unstable loops, as expected in the circuit in Fig. 4(a). To account for the complete structure, instead of using closed-loop transfer functions, we will calculate the circuit characteristic determinant [39] in a way that ensures that it cannot exhibit any RHS poles. In comparison with the well-established methods [39]-[40] (also based on the calculation of the characteristic determinant), the one used here [27] has the advantage of not requiring access to the active-device intrinsic terminals. The stability information is in the *zeroes* of the characteristic determinant and avoiding by construction the existence of RHS poles will prevent any cancellations or quasi-cancellations. This determinant is obtained by (i) partitioning the circuit into OC-stable blocks and (ii) calculating the total impedance matrix at the N ports defined in the partition. The verification of the OC stability of the blocks will be done inside the blocks through standard pole-zero identification [34]-[38], which due to the limited size of the blocks can be applied reliably. Note that an analogous procedure with SC stable blocks and a total admittance matrix is also possible [27].

In an initial test, the passive linear network considered in the circuit of Fig. 4(a) contains the ring-shaped stepped-impedance resonator only, and the active blocks are constituted by the remaining components of the two sub-oscillators. Thus, we start with $N = 2$ ports, corresponding to those denoted as Ref$_2$ and Ref$_4$ in Fig. 4(a). However, the defined active blocks are unstable when terminated in open circuits (OCs) at Ref$_2$ and Ref$_4$, respectively. As a result, we have to consider additional ports in the two active blocks: the first (second) active block has now the ports Ref$_1$ and Ref$_2$ (Ref$_3$ and Ref$_4$). When terminating the first active block in OC at Ref$_1$ and Ref$_2$, it becomes stable for all the V_{GS} values. This has been verified through pole-zero identification inside the block, at different observation nodes. Fig. 6(a) presents the variation of the real part of the dominant poles of the first active block versus V_{GS2}. All the poles have a negative real part so the block is OC stable. Likewise, when terminating the second active block in OC at Ref$_3$ and Ref$_4$, it becomes stable [Fig. 6(b)] for all the V_{GS} values. If the active blocks had still been unstable, one would have needed more analysis ports. Thus, the number of ports only depends on the active blocks and their stability properties. The stability analysis of

the whole structure (including the passive linear network) is addressed calculating the total impedance matrix at Ref$_1$, Ref$_2$, Ref$_3$ and Ref$_4$. The determinant of this total impedance matrix is:

$$\det(s) = \det \left\{ \begin{bmatrix} Z_{1,11}(s) & Z_{1,12}(s) & 0 & 0 \\ Z_{1,21}(s) & Z_{1,22}(s) & 0 & 0 \\ 0 & 0 & Z_{2,11}(s) & Z_{2,12}(s) \\ 0 & 0 & Z_{2,21}(s) & Z_{2,22}(s) \end{bmatrix} + \begin{bmatrix} z_{11}(s) & z_{12}(s) & z_{13}(s) & z_{14}(s) \\ z_{21}(s) & z_{22}(s) & z_{23}(s) & z_{24}(s) \\ z_{31}(s) & z_{32}(s) & z_{33}(s) & z_{34}(s) \\ z_{41}(s) & z_{42}(s) & z_{43}(s) & z_{44}(s) \end{bmatrix} \right\} = 0 \quad (10)$$

where s is the complex frequency, the boxes in the left matrix correspond to the impedance matrices of the 2x2 active blocks and $[z_{ij}]$ is the impedance matrix of the entire remaining passive linear part (including the ring resonator). Provided that the two active sub-circuits are stable under OC terminations, the determinant function (10) cannot exhibit any RHS poles. This is because none of the Z parameters in the active-block impedance matrix can have poles on the RHS since each of these parameters constitutes a particular closed-loop transfer function, calculated under OC terminations. Obviously, the matrix describing the passive linear network cannot exhibit any RHS poles either. In practice one directly calculates the total impedance matrix, with no need for the decomposition in (10), considered only for demonstration purposes. Note that avoiding, by construction, the coexistence of RHS zeroes and poles prevents the risk of missing instabilities.
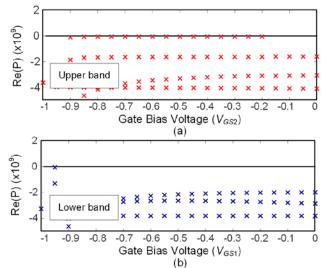

Fig. 6. Stability analysis of the two-port active blocks considered in Fig. 4 when terminated in open circuits, through standard pole-zero identification. (a) Active block with the two ports Ref$_1$ and Ref$_2$. Variation of the real part of the dominant poles versus V_{GS2}. (b) Active block with the two ports Ref$_3$ and Ref$_4$. Variation of the real part of the dominant poles versus V_{GS1}.

Fig. 7(a) presents the results of the identification of $\det(j\omega)$ when the gate-bias voltages of the two transistors are $V_{GS1} = -0.35$ V and $V_{GS2} = -0.55$ V. Remember that when using the characteristic determinant the stability information is in the zeroes. It shows two pairs of complex-conjugate zeroes in the RHS, about the two expected oscillation frequencies $f_1 = 2.49$ GHz and $f_2 = 4.22$ GHz. The result is compared with two distinct analyses through pole-zero identification of the whole structure, in the two different

sections of the circuit. Each identification [Fig. 7(b) and Fig. 7(c)] detects a single pair of RHS complex-conjugate poles at the corresponding oscillation frequency. Thus, the standard pole-zero identification is unable to capture the stability properties of the whole structure. Fig. 7(d) presents the evolution of the real part of the zeroes of det(s) when varying V_{GS1} at constant $V_{GS2} = -0.55$ V. The second sub-oscillator [associated with Section 2 in Fig. 4(a)] is always unstable, so for all the values of V_{GS1}, there is a pair of complex-conjugate zeroes in the RHS. The pole-zero identification is unable to detect this additional pair of RHS poles.
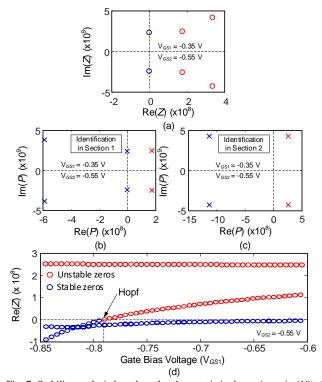

Fig. 7. Stability analysis based on the characteristic determinant in (10). (a) Identification of det($j\omega$) for $V_{GS1} = -0.35$ V and $V_{GS2} = -0.55$ V. The stability information is in the zeroes. (b) Pole-zero identification in Section 1 for the same conditions. The stability information is in the poles. (c) Pole-zero identification in Section 2 for the same conditions. (d) Variation of the real part of the dominant zeroes of det(s) at constant $V_{GS2} = -0.55$ V.

C. Stability of the periodic solutions

A common problem in concurrent dual-frequency oscillators is the coexistence [8] of the doubly-autonomous quasi-periodic solution (having ω_1 and ω_2 as the two fundamental frequencies), with stable periodic solutions at ω_1 and/or ω_2 (and no concurrency). For the stability analysis of these periodic solutions, an AG [23] will be introduced in the circuit section (1 or 2) exhibiting the oscillation. The periodic solution at ω_1 (ω_2) is analyzed by setting the AG frequency to this value, doing $\omega_{AG} = \omega_1$ ($\omega_{AG} = \omega_2$). Then, the AG amplitude V_{AG} and ω_{AG} will be optimized to fulfil $Y_{AG} = 0$, where Y_{AG} is the ratio between the AG current and amplitude. In the particular case of the circuit in Fig. 4, the AG is connected in parallel at the source terminal. Once the free-running oscillation of Section 1 (2) is obtained, the stability analysis of this solution is carried out through standard pole-zero identification [34]-[38], introducing a small-signal current generator in Section 2 (1), which is the one prone to oscillate at the frequency ω_2 (ω_1). Fig. 8(a) shows the variation versus the gate-bias voltage V_{GS2} of the real part of the dominant poles (calculated through identification in

Section 2) when Section 2 exhibits a steady-state periodic oscillation at $f_1 \cong 2.4$ GHz. In turn, Fig. 8(b) shows the variation versus V_{GS1} of the real part of the dominant poles (calculated through identification in Section 2) when Section 1 exhibits a steady-state periodic oscillation at $f_2 \cong 4.1$ GHz. The oscillation in each section is never stable if the other section has surpassed the oscillation threshold determined with the DC stability analysis described in the previous subsection. Compare the crossing of the poles in Fig. 8(b), with Section 1 in an *oscillatory* state, with the crossing of the zeroes in Fig. 7(d), with Section 1 in a *non-oscillatory* state. The crossing to the RHS takes place for approximately the same value of V_{GS1}. In fact, the Hopf bifurcation from DC regime [21]-[25] takes place at $V_{GS1} = -0.791$ V and the (secondary) Hopf bifurcation from a periodic regime takes place at $V_{GS1} = -0.794$ V. In each case and due to the high isolation between Section 1 and Section 2, standard pole-zero identification is unable to detect the pair of poles in the imaginary axis, associated with the steady-state oscillation in the other section.
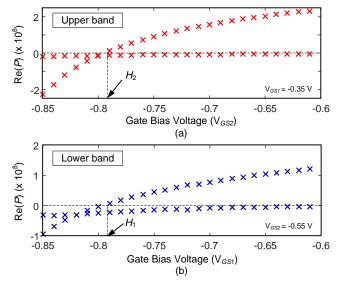

Fig. 8. Stability analysis of the periodic oscillations at ω_1 and ω_2. The Hopf bifurcations H_1 and H_2 take place at $V_{GS1} = -0.791$ V and $V_{GS2} = -0.794$ V respectively.

D. Stability of the quasi-periodic oscillation

To obtain the concurrent doubly autonomous quasi-periodic oscillation, two AGs are introduced into the circuit, one per sub-oscillator. They are connected at the source terminals of the two transistor devices and operate at the frequencies $\omega_{AG1} = \omega_{o1}$ and $\omega_{AG2} = \omega_{o2}$, with the respective amplitudes V_{AG1} and V_{AG2}. In the presence of these two AGs, the circuit is analyzed with two-tone HB, at the two incommensurable oscillation frequencies $\omega_{AG1} = \omega_{o1}$ and $\omega_{AG2} = \omega_{o2}$. The two AG frequencies and amplitudes ω_{AG1}, ω_{AG2}, V_{AG1} and V_{AG2} are simultaneously optimized in order to fulfil $Y_{AG1} = 0$ and $Y_{AG2} = 0$, where Y_{AGi} ($i = 1,2$) is the current-to-voltage ratio at each of the two generators. The oscillation is ideally suppressed at the circuit output, containing an open-circuited $\lambda/4$ stub at the oscillation frequency. Thus, the spectrum in each sub-oscillator has been simulated and measured at the input terminal (Fig. 9). The two oscillations are concurrent, very robust and exhibit a good isolation.

The stability of the doubly autonomous quasi–periodic solution is analyzed linearizing the two outer–tier admittance functions Y_{AG1} and Y_{AG2} about this quasi–periodic steady–

state solution, as done in [8]. This provides four Lyapunov exponents [21]-[22]. Two of them are zero due to the double autonomy of this solution [21]. The other two exponents, $\lambda_{1,2}$, determining the stability properties, are [8]:

$$\lambda_{1,2} = \frac{a_{11} + a_{22}}{2} \pm \frac{\sqrt{(a_{11} - a_{22})^2 + 4a_{12}a_{21}}}{2} \quad (11)$$

where:

$$a_{11} = \frac{-\left(\dfrac{\partial Y_{T1}^r}{\partial V_1}\dfrac{\partial Y_{T1}^i}{\partial \omega_1} - \dfrac{\partial Y_{T1}^r}{\partial \omega_1}\dfrac{\partial Y_{T1}^i}{\partial V_1}\right)}{\left|\partial Y_{T1}/\partial \omega_1\right|^2}, \quad a_{12} = \frac{-\left(\dfrac{\partial Y_{T1}^r}{\partial V_2}\dfrac{\partial Y_{T1}^i}{\partial \omega_1} - \dfrac{\partial Y_{T1}^r}{\partial \omega_1}\dfrac{\partial Y_{T1}^i}{\partial V_2}\right)}{\left|\partial Y_{T1}/\partial \omega_1\right|^2}$$

$$a_{21} = \frac{-\left(\dfrac{\partial Y_{T2}^r}{\partial V_1}\dfrac{\partial Y_{T2}^i}{\partial \omega_2} - \dfrac{\partial Y_{T2}^r}{\partial \omega_2}\dfrac{\partial Y_{T2}^i}{\partial V_1}\right)}{\left|\partial Y_{T2}/\partial \omega_2\right|^2}, \quad a_{22} = \frac{-\left(\dfrac{\partial Y_{T2}^r}{\partial V_2}\dfrac{\partial Y_{T2}^i}{\partial \omega_2} - \dfrac{\partial Y_{T2}^r}{\partial \omega_2}\dfrac{\partial Y_{T2}^i}{\partial V_2}\right)}{\left|\partial Y_{T2}/\partial \omega_2\right|^2}$$

All the derivatives of the admittance functions are calculated applying finite differences to the two AGs used to obtain the doubly autonomous quasi-periodic solution, as explained in [8]. The two circuit sections in Fig. 4(a) would be fully isolated for $a_{12} = 0$ and $a_{21} = 0$ and the two Lyapunov exponents would become $\lambda_1 = a_{11}$ and $\lambda_2 = a_{22}$. Thus, the coefficients a_{12} and a_{21} give a measure of the connectivity between the two circuit sections. Fig. 10(a) presents the variation of the doubly-autonomous quasi-periodic solution, in terms of the oscillation amplitude at the source terminal in Section 1 and Section 2, versus V_{GS1} for $V_{GS2} = -0.55$ V. The oscillation at the lower band has very low impact on the oscillation at the upper band. Fig. 10(b) shows the variation of a_{12} and a_{21} through the solution curve in (a). The larger values are comprised in the interval $V_{GS1} = -0.75$V to $V_{GS1} = -0.8$ V, which agrees with the one in which the oscillation in the lower band has the strongest effect on the upper-band oscillation. Fig. 10(c) shows the variation of the two exponents λ_1 and λ_2 versus V_{GS1}. As expected, one of the two exponents (λ_1) becomes zero at $V_{GS1} = -0.82$ V where the oscillation at the lower frequency is extinguished. The doubly-autonomous quasi-periodic solution is stable for all the V_{GS1} values, as validated experimentally. Fig. 10(d) presents the measurements at the input terminal in concurrent mode. Remember that the oscillation is ideally suppressed at the circuit output.
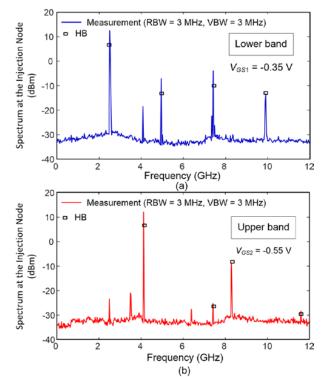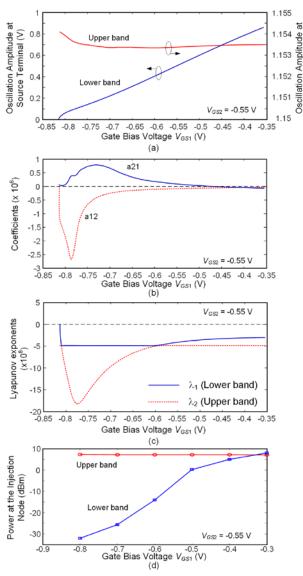

Fig. 9. Doubly-autonomous quasi-periodic solution. Simulated and measured spectrum at each of the two sub-oscillators, biased at $V_{GS1} = -0.35$ V and $V_{GS2} = -0.55$ V, respectively. (a) Lower-frequency oscillator. (b) Upper-frequency oscillator.

Fig. 10. Stability of the doubly-autonomous quasi-periodic solution. (a) Variation of oscillation amplitude at the source terminal in Section 1 (lower band) and in Section 2 (upper band), versus V_{GS1} for V_{GS2} = -0.55 V. (b) Variation of a_{12} and a_{21} through the solution curve in (a). (c) Variation of the two exponents λ_1 and λ_2 versus V_{GS1}. (d) Experimental validation of the stable behavior versus V_{GS1}.

IV. HETERODYNE SOM

As shown in Section II, an heterodyne SOM mixes the input signal at the frequency ω_{in} with a self-generated incommensurable oscillation at the frequency ω_o to provide an intermediate signal at the frequency ω_{IF}. In the concurrent dual-band SOM, the mixing takes place simultaneously in the two sub-oscillators, so, in principle, the analysis of this regime requires two auxiliary generators at the respective frequencies $\omega_{AG1} = \omega_1$ and $\omega_{AG2} = \omega_2$. However, due to the good isolation, demonstrated in Section III, it will be possible to optimize each sub-oscillator independently.

A. Gain optimization

To optimize the gain of the heterodyne SOM, linear operation with respect to the input source will be initially considered, so the circuit can be linearized about the free-running solution obtained with the HB system [24]-[25]:

$$\overline{H}_k(\overline{V}, \overline{\mu}) = \left[A_V(k\omega_o)\right]\overline{V}_k + \left[A_{yN}(k\omega_o)\right]\overline{F}_k(\overline{V}) +$$

$$\left[A_{gN}(k\omega_o)\right]\overline{G}_k = 0 \qquad \text{(a)} \qquad (12)$$

$$Y_{AG}(V_{AG}, \omega_o, \overline{\mu}) = \frac{I_{AG}}{V_{AG}} = 0 \qquad \text{(b)}$$

where $\overline{H}_k(\overline{V}, \overline{\mu})$ with $-NH \leq k \leq NH$ is the set of error equations, depending on the vector $\overline{\mu}$ of analysis parameters (bias voltages and particular element values, for instance) and the whole set of harmonic components $\overline{V}$ of the control voltages of the nonlinear elements $\overline{F}(\overline{V})$, and $\overline{G}$ is the vector of independent sources. The matrices $\left[A_V(k\omega_o)\right]$ $\left[A_{yN}(k\omega_o)\right]$ and $\left[A_{gN}(k\omega_o)\right]$ account for the passive linear elements and respectively relate the control voltages $\overline{V}$ with $\overline{F}(\overline{V})$ and $\overline{G}$; their role is identical to that of A_y and A_g in (2). Because the aim is to obtain the free-running solution, the vector $\overline{G}$ of independent generators does not include the RF input source. It contains the DC sources and an AG, with amplitude V_{AG}, at ω_o. By fulfilling (12)(b), this AG prevents the undesired convergence to the coexistent DC solution. Now we consider a small RF input signal at $\omega_o + \Omega$, where Ω is IF frequency. In the presence of this small input signal, the HB system can be linearized about the free-running solution obtained through (12) with the conversion-matrix approach [41], which provides:

$$\left[A_V(k\omega_o + \Omega)\right]\Delta\overline{V}_k(k\omega_o + \Omega) \sum_{l=-NH}^{l=NH} \left[A_{yN}(k\omega_o + \Omega)\right]\frac{\partial\overline{F}_k}{\partial\overline{V}_l}\Delta\overline{V}_l +$$

$$\left[A_{gN}(k\omega_o + \Omega)\right]\overline{G}_{ss}(k\omega_o + \Omega) = 0$$

$$(13)$$

where $-NH \leq k \leq NH$ and the small RF signal is included in the vector $\overline{G}_{ss}$ that fulfills $\overline{G}_{ss}(k\omega_o + \Omega) = 0$ for $k \neq 1, -1$. Under any variation of $\overline{\mu}$, one solves sequentially (12) and (13) to obtain the conversion gain G_{IF} as the ratio between the output power at Ω and the available power at $\omega_{in} + \Omega$.

The two equations (12) and (13) have been used to select the values of the IF filter elements, L_i, C_i, where i = 1, 2, that maximize G_{IF}. Thus, the vector $\overline{\mu}$ contains, in each sub-oscillator, the elements L_i, C_i. The analysis has been carried out keeping the gate-bias voltages at their original values V_{GS1} = -0.35 V and V_{GS2} = -0.55 V since the impact of the bias conditions on the conversion gain and linearity is studied in later in this section. For the constant offset frequency $f_{IF} = \Omega/(2\pi)$ =100 MHz, agreeing with the desired intermediate frequency, one obtains the constant-gain contours shown Fig. 11. The contours in Fig. 11(a) [(b)] correspond to the sub-oscillator at 2.4 GHz (4.1 GHz). As gathered from these contours, G_{IF} strongly depends on the values of the IF output network, which affect both the filtering and impedance matching at the IF frequency. The operation points selected are indicated in the figure. Note that the sub-oscillator at 2.4 GHz is able to exhibit higher gain at lower IF. At 2.4 GHz, the measured conversion gain for the values indicated in Fig. 7 are -2.7 dB at the IF frequency 100 MHz and 7 dB at 70 MHz. At the upper frequency, the measured conversion gain is 3.3 dB at 100 MHz.
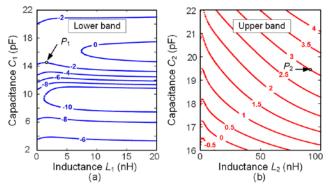
Fig. 11. Constant gain contours in the heterodyne SOM at the intermediate frequency at 100 MHz. (a) Lower band (2.4 GHz). (b) Upper band (4.1 GHz).

B. Nonlinear response versus the input power

After the optimization of the linear conversion gain of the heterodyne SOM, this circuit will be analysed in nonlinear regime with respect to the input source. This is done introducing the RF input source in the vector $\bar{G}$ of (12)(a) and considering two fundamental frequencies: ω_{in} and ω_o. The AG is maintained for this analysis and must fulfil $Y_{AG} = 0$ in the presence of the input source, which avoids the undesired convergence to a trivial periodic solution at ω_{in}. The solution curve versus a given parameter η can be traced through AG optimization in two-tone HB, at ω_{in} and $\omega_{AG} = \omega_o$, which would be done sweeping η and optimizing ω_o and V_{AG} at each step [42]. However, due to the usual complexity of the solution curves, exhibiting turning points [23] that demand several manual parameter switches [18], [26], an extension of the contour-intersection method [19]-[20] to the SOM regime has been carried out. This method enables an exhaustive search of coexisting solutions, with no need for continuation procedures. It also relies on the use of an AG, though this AG is not optimized, but introduced to obtain a nonlinear admittance function, as described in the following.

For each η, a double sweep is performed in V_{AG} and ω_{AG} in two-tone HB, at ω_{in} and ω_{AG}. For each pair of values V_{AG} and ω_{AG} one calculates Y_{AG}, as the ratio between the AG current and voltage, as well as the conversion gain G_{IF}. Then, three surfaces are obtained: S_{Re} in the space V_{AG}, ω_{AG}, $Re(Y_{AG})$, S_{Im}, in the space V_{AG}, ω_{AG}, $Im(Y_{AG})$ and S_{GIF}, in the space V_{AG}, ω_{AG}, G_{IF}. The surfaces S_{Re} and S_{Im} are used to obtain the solution points, whereas the surface S_{GIF} is used to obtain the conversion gain at these solution points. The intersection of the surface S_{Re} with the plane $Re(Y_{AG}) = 0$ provides the curve C_{Re}. Likewise, the intersection of the surface S_{Im} with the plane $Im(Y_{AG}) = 0$ provides the curve C_{Im}. Fig. 11(a) presents several of these curves, obtained when varying $\eta = P_{in}$ in the suboscillator at the upper frequency, for the selected intermediate frequency 100 MHz. The curves C_{Re} and C_{Im} can be expressed as:

$$C_{Re}(V_{AG}, \omega_{AG}) = S_{Re}(V_{AG}, \omega_{AG}) \cap \{Re[Y_{AG}] = 0\}$$
$$C_{Im}(V_{AG}, \omega_{AG}) = S_{Im}(V_{AG}, \omega_{AG}) \cap \{Im[Y_{AG}] = 0\} \quad (14)$$

Then, all the coexisting solution points for the particular parameter value η are given by the intersection points of C_{Re} and C_{Im}, that is:

$$P = C_{Re} \cap C_{Im} \quad (15)$$

where P is a discrete set containing the solution points. Fig. 12(a) presents the collection of intersection points obtained when varying the input power, $\eta = P_{in}$, in the sub-oscillator

at the upper frequency. Representing the points P in (15) versus P_{in} one obtains the solution curve [Fig. 12(a)] in terms of V_{AG} (agreeing with the voltage amplitude at the node where the AG is connected) and ω_{AG} (agreeing with the oscillation frequency). For low P_{in}, there is a negligible variation of ω_{AG} and V_{AG}, and the solutions accumulate at the point surrounded with a circle.
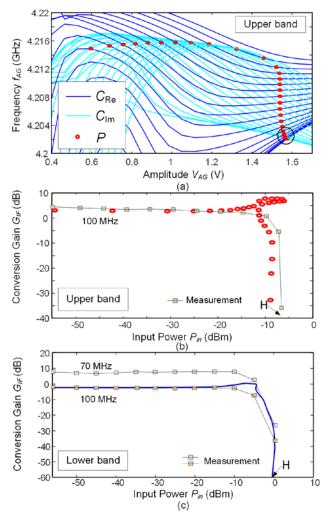

Fig. 12. Contour-intersection method. (a) Collection of intersection points $P(P_{in})$ obtained when varying P_{in} in the sub-oscillator at the upper frequency. (b) Conversion gain G_{IF} versus P_{in} obtained through the interpolation of the surface $S_{GIF}(P_{in})$ at the solution points $P(P_{in})$ of (a). The Hopf bifurcation takes place at $P_{in} = -8.9$ dBm. (c) Lower band. The Hopf bifurcation takes place at $P_{in} = -1.2$ dBm.

To obtain the variation of the conversion gain G_{IF} versus η, one should interpolate the surface $S_{GIF}(\eta)$ at the solution points $P(\eta)$. In our case, this interpolation must be carried out at the points resulting from the intersections in Fig. 12(a). For $f_m = 100$ MHz, the curve providing G_{IF} versus P_{in} is shown in Fig. 12(b). Experimental measurements are also represented with good agreement. Fig. 12(c) presents the variation of G_{IF} in the lower-frequency sub-oscillator. Two IF frequencies are considered: 70 MHz and 100 MHz (compared with the simulation results). As seen in Fig. 12(b) and (c), the gain remains constant at the small-signal value up to certain P_{in}, then there is a small interval of gain expansion and an abrupt decay as the oscillation amplitude tends to zero at the Hopf bifurcation H. This form of gain variation is fully explained by the analytical model in (2) to (6) of Section II. As also understood from this model, the device bias point should be

suitably chosen since, besides a sufficient quadratic response, one must ensure enough oscillation amplitude. We have analysed the conversion gain versus V_{GS} for P_{in} = -36 dBm and P_{in} = -16 dBm with the results shown in Fig. 13(a), where experimental points are superimposed. When reducing V_{GS} towards pinch-off, there is an interval of irregular behaviour until the oscillation is eventually extinguished at the Hopf bifurcation H. Thus, one should avoid too low V_{GS}. Fig. 13(b) shows a more detailed analysis of the conversion gain in a narrower V_{GS} interval, considering multiple P_{in} values comprised between P_{in} = -36 dBm and P_{in} = -16 dBm. Higher linearity is expected for the V_{GS} at which all the gain points are (nearly) overlapped. For comparison, the oscillation amplitude V_o is also represented in Fig. 13(b).
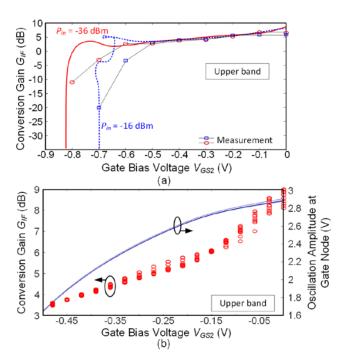

Fig. 13. Effect of the gate-bias voltage on the conversion gain of the heterodyne SOM. (a) Conversion gain in a broad V_{GS} interval for two input power values P_{in} = -36 dBm and P_{in} = -16 dBm. Measurement points are superimposed. (b) Conversion gain in a narrower V_{GS} interval for multiple P_{in} values. The oscillation amplitude is also represented for comparison.

The previous analyses have been carried out considering only the oscillation occurring in each particular circuit section: that is, using only one AG, connected to that section, and leaving the other section in a non-oscillatory state. However, we have also verified the proper SOM behaviour when considering the two concurrent oscillations, by using two AGs, one connected to each circuit section. Assuming an identical IF frequency, ω, for the two suboscillators, the analysis can be carried out with three-tone HB at ω_1, ω_2 and ω. A variation of P_{in} in any of the two sub-oscillators has no impact on the IF output at the other sub-oscillator, as shown in Fig. 14, where the input power corresponding to the upper-band oscillator has been increased from -36 dBm to -16 dBm, while leaving the input power at the lower-band oscillator constant, at P_{in} = -36 dBm. There is an excellent agreement with the experimental results.
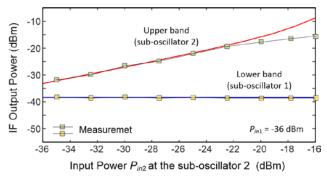

Fig. 14. Concurrent operation of the heterodyne SOM under an identical IF frequency of 100 MHz in the two suboscillators. Evolution of the IF output in these two sub-oscillators when increasing the input power at the upper band from -36 dBm to -16 dBm, while holding the input power at the lower band constant at P_{in} = -36 dBm.

C. Intermodulation

The intermodulation distortion of the SOM will be analyzed considering two closely spaced input tones about ω_{in}. The analysis is carried out with the envelope-transient method [18], representing the two input tones as a modulation of the carrier ω_{in}. Two fundamental frequencies are considered in the Fourier series representation of the circuit variables: ω_{in} and ω_o, where ω_o is the self-oscillation frequency in the presence of the non-modulated input source, obtained through HB with the aid of an AG (optimized to fulfill $Y_{AG} = 0$). When the modulation due to the two input tones is introduced, the control voltages become time varying $\bar{V}(t)$ and, provided that the frequency spacing is sufficiently small in comparison with the carrier frequencies, one can expand the matrices $\left[A_y \right]$ and $\left[A_g \right]$ in a Taylor series about $(k\omega_o + l\omega_{in})$, in a manner similar to what was done in equation (8). Taking into account that the frequency increments act like time differentiators, one obtains:

$$\left[A_V(k\omega_o + l\omega_{in}) \right] \bar{V}_{k,l}(t) - j \frac{\partial \left[A_V(k\omega_o + l\omega_{in}) \right]}{\partial \omega} \dot{\bar{V}}_{k,l}(t) +$$
$$\left[A_{yN}(k\omega_o + l\omega_{in}) \right] \bar{F}_{k,l}\left(\bar{V}(t) \right) +$$
$$- j \frac{\partial \left[A_{yN}(k\omega_o + l\omega_{in}) \right]}{\partial \omega} \dot{\bar{F}}_{k,l}\left(\bar{V}(t) \right) +$$
$$\left[A_{gN}(k\omega_o + l\omega_{in}) \right] \bar{G}_{k,l}(t) - j \frac{\partial \left[A_{gN}(k\omega_o + l\omega_{in}) \right]}{\partial \omega} \dot{\bar{G}}_{k,l}(t) = 0$$

(16)

where $-NH \le k \le NH$. As in (8), it would be possible to consider higher order terms in the Taylor expansion. The oscillation is initialized connecting the AG to the circuit at the initial time t_o only. This is done introducing a resistor $R_{AG}(t)$ in series with the AG, as shown in Fig. 4(a). This resistor has zero value at the initial time $t = t_o$ and very large value, ideally infinite, at $t > t_o$, which disconnects the AG from the circuit. For the analysis of the intermodulation spectrum, the time interval in steady-state regime must be long enough to ensure a sufficient accuracy in the Fourier transform. Fig. 15(a) compares the simulated and measured output spectrum in the upper band when the power of the two input tones is -30 dBm. The bias voltages are in the region of less sensitivity of the conversion gain with respect to P_{in} in Fig. 13(b). The gain is 3.3 dB and the carrier to intermodulation ratio (C/I) is 42.8 dB. In the lower band (at f_m = 70 MHz), the gain is 7 dB and

the C/I is 44.6 dB as can be seen in the measured output spectrum in Fig. 15(b).
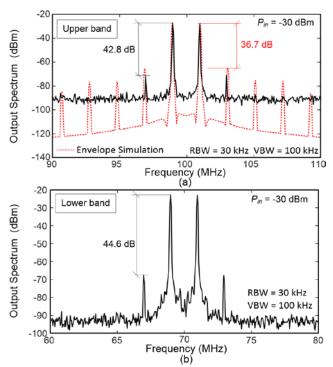

Fig. 15. Heterodyne SOM. Intermodulation behaviour for P_{in} = -30 dBm. Output spectrum obtained with envelope transient when the input signal is constituted by two tones with the frequency spacing 2 MHz. (a) Upper band (simulated and measured). (b) Lower band (measured).

D. Noise analysis

The SOMs are generally intended for compact low-cost applications in which the oscillation is not locked to a reference, so one should minimize the phase noise of this oscillation. The intermediate frequency of the heterodyne SOM is $\omega_{in} - \omega_o$, so the phase noise at the oscillation frequency ω_o will have a direct impact on the IF signal. The noise analysis of the SOM will be carried out with an outer-tier procedure, connecting two AGs at the transistor gate terminal, each at one of the two fundamental frequencies ω_{in} and ω_o. The AG at ω_{in} has the amplitude V_i and phase shift with respect to the input source ϕ_i. The AG at ω_o has the amplitude V_o. For a given input amplitude E_{in} and frequency ω_{in}, the two AGs are simultaneously optimized to fulfill:

$$Y_o(V_o, \omega_o, V_i, \phi_i) = 0$$
$$Y_i(V_o, \omega_o, V_i, \phi_i) = 0 \qquad (17)$$

where the dependence on E_{in} is implicit. In fact, the above two equations play a role similar to those in (2), though in (17) the rest of circuit variables are considered in the HB system that constitutes an inner tier. Now the effect of the noise sources will be considered. The phase perturbation of the input source at ω_{in} is $\psi(t)$ and the equivalent noise sources at ω_{in} and ω_o are I_{Ni} (including the input amplitude noise) and I_{No}. Because the noise perturbations are small, one can expand the nonlinear functions Y_i and Y_o in a first-order Taylor series applying finite differences [43] to the two AGs. After suppressing the steady-state terms, one obtains a perturbation system in the four increments $\delta V_i, \delta \phi_i, \delta V_o, \delta \phi_o$ of the respective variables V_i, ϕ_i, V_o, ϕ_o:

$$\frac{\partial Y_i}{\partial V_i} \delta V_i + \frac{\partial Y_i}{\partial \phi_i} \delta \phi_i + \frac{\partial Y_i}{\partial \omega_{in}} \left(\delta \dot{\phi}_i - j \frac{\delta \dot{V}_i}{V_i} + \dot{\psi} \right) + \frac{\partial Y_i}{\partial V_o} \delta V_o +$$

$$\frac{\partial Y_i}{\partial \omega_o} \left(\delta \dot{\phi}_o - j \frac{\delta \dot{V}_o}{V_o} \right) = \frac{I_{Ni}(t)}{V_i e^{j\phi_i}} \qquad (a) \quad (18)$$

$$\frac{\partial Y_o}{\partial V_i} \delta V_1 + \frac{\partial Y_o}{\partial V_o} \delta V_o + \frac{\partial Y_o}{\partial \omega_o} \left(\delta \dot{\phi}_o - j \frac{\delta \dot{V}_o}{V_o} \right) = \frac{I_{No}(t)}{V_o} \qquad (b)$$

where it has been considered that the complex-frequency increments give rise to a time differentiation of the amplitude and phase increments [44]. In the usual case of a low-noise input source, one can simplify (17) considering that $\psi(t)$ will be much smaller than the oscillation phase noise and may also disregard the derivatives $\delta \dot{V}_i, \delta \dot{\phi}_i$. Splitting the two complex equations into real and imaginary parts and applying the Fourier transform, one obtains:

$$S(\Omega) = M^{-1}(\Omega) N(\Omega) \left(M^{-1}(\Omega) \right)' \qquad (19)$$

where $S(\Omega)$ is the correlation matrix of the noise perturbations, $N(\Omega)$ is that of the noise sources and the matrix $M(\Omega)$ is given by:

$$M(\Omega) = \begin{bmatrix} \dfrac{\partial Y_i^r}{\partial V_i} & \dfrac{\partial Y_i^r}{\partial \phi_i} & j\Omega \dfrac{\partial Y_i^i}{\partial \omega_o} \dfrac{1}{V_o} + \dfrac{\partial Y_i^r}{\partial V_o} & j\Omega \dfrac{\partial Y_i^r}{\partial \omega_o} \\[3mm] \dfrac{\partial Y_i^i}{\partial V_i} & \dfrac{\partial Y_i^i}{\partial \phi_i} & -j\Omega \dfrac{\partial Y_i^r}{\partial \omega_o} \dfrac{1}{V_o} + \dfrac{\partial Y_i^i}{\partial V_o} & j\Omega \dfrac{\partial Y_i^i}{\partial \omega_o} \\[3mm] \dfrac{\partial Y_o^r}{\partial V_i} & 0 & j\Omega \dfrac{\partial Y_o^i}{\partial \omega_o} \dfrac{1}{V_o} + \dfrac{\partial Y_o^r}{\partial V_o} & j\Omega \dfrac{\partial Y_o^r}{\partial \omega_o} \\[3mm] \dfrac{\partial Y_o^i}{\partial V_i} & 0 & -j\Omega \dfrac{\partial Y_o^r}{\partial \omega_o} \dfrac{1}{V_o} + \dfrac{\partial Y_o^i}{\partial V_o} & j\Omega \dfrac{\partial Y_o^i}{\partial \omega_o} \end{bmatrix} \quad (20)$$

where the superscripts indicate real and imaginary parts. The matrix $N(\Omega)$ contains the spectral densities of I_{Ni} and I_{No}. The spectral density of I_{Ni} is approached as $4G_s kT_o$, where k is the Boltzamn constant, G_s the real part of the source admittance seen from the gate terminal and $T_o = 290°$ K. The values are $|I_{N1}|^2 = 8\ 10^{-23}$ A^2/Hz, $|I_{N2}|^2 = 1.1\ 10^{-22}$ A^2/Hz, for the first and second suboscillator, respectively. On the other hand, the spectral density of I_{No} is obtained by fitting [43] the phase-noise spectrum obtained through circuit-level simulations [45] with the one resulting from the noise perturbation of $Y_o(V_o, \omega_o) = 0$ (in the absence of the input source). The spectral density of I_{No} contains both white noise and upconverted flicker-noise contributions. In the first suboscillator it is $|I_{No1}|^2 = (0.27\ 10^{-20} + 3\ 10^{-13}/f)$ A^2/Hz. In the second suboscillator it is $|I_{No2}|^2 = (0.3\ 10^{-20} + 5\ 10^{-13}/f)$ A^2/Hz. Solving (19), one obtains the phase and amplitude noise at the two fundamental frequencies ω_o and ω_{in} of the quasi-periodic solution. The analysis has been carried out at both the lower band [Fig. 16(a)] and upper band [Fig. 16(b)]. The phase noise $|\delta \phi_o|^2$ at the oscillation frequency has been represented with black dots. Of all the rest of noise contributions resulting from (18) to (20), the dominant one is the amplitude noise associated with δV_i, which has also been traced with black dots. This dominance of the noise associated with δV_i can be understood with the formulation (19)-(20). When solving for δV_i using the matrix in (20), the derivatives of the admittance functions with respect to V_i appear in the denominator only,

unlike what happens with the rest of perturbed variables. Under rather small input amplitude E_{in}, these derivatives will be much smaller than the ones with respect to V_o and ϕ_1, which explains the relatively large value of the amplitude noise at the input frequency. The results have been compared with the experimental measurements using the Rohde & Schwarz FSWP8- Phase Noise Analyzer. The black and blue traces correspond to the experimental measurements of the phase-noise spectrum at the oscillation frequency ω_o and the IF frequency $\omega_{in}-\omega_o$, respectively. At the lower offset frequencies, the two traces are nearly coincident. The phase noise predicted through (19) at ω_o (represented with black dots) exhibits a very good agreement. Thus, at low offset frequencies the phase noise at IF basically agrees with that of the self-oscillation. At larger offset frequency, the two phase-noise spectra exhibit a different form of variation. The phase-noise at the oscillation frequency keeps decreasing with the same -20 dB/dec slope. In contrast, the phase noise at IF approaches the amplitude noise associated with δV_i, which, in turn, is very similar to the amplitude noise measured at IF frequency. The relevance of this amplitude noise at the IF frequency is attributed to the down conversion action. The corner from which the phase-noise spectrum flattens depends on the intensity of this amplitude noise. For completeness, the spectrum at both the lower and upper bands in injection-locked conditions has also been represented.
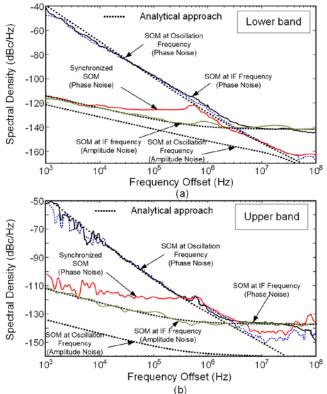

Fig. 16. Heterodyne SOM. Experimental phase and amplitude noise at the oscillation frequency and the intermediate frequency. Results obtained with the analytical approach are also represented. (a) Lower band. (b) Upper band.

V. Zero-IF SOM

For operation as a Zero-IF SOM, the circuit self-oscillation must be injection-locked by an input signal, as shown in Section II.B. The investigation here will focus on three aspects of the transistor-based implementation of Fig. 4: the operation bands as a zero-IF mixer, the linear gain analysis, and the behaviour under modulation signals [1].

A. Operation bands

Initially, the impact of one oscillator on the other will be neglected. The analysis of each injection-locked sub-oscillator will be carried out with one-tone HB at the corresponding input frequency ω_{in}. The solution curves, which should be analogous to those in Fig. 3 of Section II, are obtained through the contour-intersection method in [19], based on a two-stage procedure. The first step is a separate simulation of the passive-linear input network defined between the input source and the analysis node (gate terminal), to obtain its Norton equivalent current $I_N(\omega)$ at each input frequency. This analysis should provide the scattering matrix $[S]$ of the input network. The second step is the extraction of a nonlinear admittance function $Y_{AG}(V_{AG}, \omega_{AG})$ at the analysis terminal using an AG connected to this terminal. The purpose of this function is conceptually similar to that of the function Y_{AG} in Section IV.B. The function is calculated by performing a double sweep in the AG frequency ω_{AG} and amplitude V_{AG} and calculating, at each step, the ratio between the AG current I_{AG} and V_{AG}. Once the scattering matrix and the nonlinear admittance function have been calculated, the following relationships are used:

$$Y_{AG}(V_{AG}, \omega_{AG})V = I_N(\omega_{AG})$$

$$I_N(\omega_{AG}) = \frac{2S_{21}}{1 - S_{11} - (\Delta - S_{22})} \frac{E_{in}}{R_o} \qquad (21)$$

where S_{ij} are the scattering parameters of the input network Δ is the determinant of the scattering matrix and R_o is the input generator resistance. The two equations in (21) can be combined in a single one. Then the family of solution curves versus the input frequency is obtained defining several contour levels in terms of E_{in} [19] in the plane ω_{AG}, V_{AG}.

At the lower and upper bands, one obtains the curves in Fig. 17, traced in terms of the oscillation amplitude V at the gate terminal versus the input frequency ω, for different values of E_{in}. As in Fig. 3, the turning points in the curves obtained for the lower E_{in} values correspond to local-global bifurcations [21]-[23] at which an incommensurate oscillation arises with a zero value of the beat frequency. Note that this beat frequency grows quickly when moving away from the tuning points. It agrees with the IF frequency of the heterodyne SOM, treated in the previous section.

The closed-solution curves in Fig. 17 can also be obtained in concurrent operation, using two-tone HB, at two incommensurate frequencies, agreeing with the (separately) injection-locked oscillation frequencies. The circuit is analysed with two AGs, one in each sub-oscillator, at the respective frequencies $\omega_{AG1} = \omega_{in1}$ and $\omega_{AG2} = \omega_{in2}$. One can use a common phase variable ϕ to define the phase shift between the input source at ω_{in1} and the auxiliary generator at ω_{AG1}, and the phase shift between the input source at ω_{in2} and the auxiliary generator at ω_{AG2}. For each P_{in}, the two closed synchronization curves are simultaneously traced by sweeping the phase ϕ (which will be the same for the two sub-circuits) and optimizing the respective AG amplitudes and frequencies at each sweep step to fulfil simultaneously the two oscillation conditions $Y_{AG1} = 0$ and $Y_{AG2} = 0$. When proceeding like this for $V_{in} = 0.1$ V ($P_{in} = -16$ dBm), one obtains the solution curves represented with squares in Fig. 17(a) and Fig. 17(b). They are nearly overlapped with the

ones obtained with a single AG, which again, demonstrates the good isolation between the two sub-oscillators.
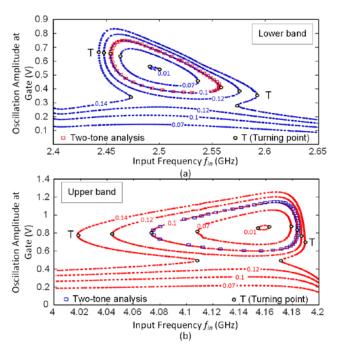

Fig. 17. Zero-IF SOM. Family of solution curves versus ω_{in} for different E_{in} values. The injection-locked curve at $E_{in} = 0.1$ V obtained through contour intersections with one AG is compared with the one obtained through a concurrent-oscillation analysis, with two AGs. (a) Lower band. (b) Upper band.

As stated, the turning points in the curves obtained for the lower input amplitude correspond to an unlocking phenomenon that leads to operation as a heterodyne SOM. Thus, the representation of these points in the plane defined by the input frequency and input amplitude will provide the boundaries between the regions in which the circuit operates as a heterodyne mixer and as zero-IF SOM. In Fig. 18(a), this representation has been carried out at the lower operation band, comparing the results with the experimental measurements. The turning-point locus is traced with blue circles. As indicated in Section II.B, for the higher input amplitudes, the onset of quasi-periodic or mixer-like solutions is due to Hopf bifurcations, at which the oscillation arises from zero amplitude, as seen in Fig. 12. The Hopf-bifurcation locus has been represented with dotted lines in Fig. 18(a). This locus can be obtained by introducing an AG into the circuit at a small-signal amplitude $A_{AG} = \varepsilon$ and frequency $\omega_{AG} = \omega$, incommensurate with the input frequency ω_{in}. Then, ω_{in} is swept, optimizing the input amplitude E_{in} and the oscillation frequency ω at each step in order to fulfil $Y_{AG}(\omega, E_{in}) = 0$, as described in [23]. The circuit operates in periodic regime inside the turning point locus and above the Hopf locus. Note that the upper section of the turning-point locus has no physical effect. Optimum operation as a zero-IF SOM would be obtained for the lower input voltages, where maximum advantage is taken of the oscillation amplitude. For illustration, Fig. 18(b) presents an experimental trace of the locking band obtained for $P_{in} = -22$ dBm using a maximum hold.
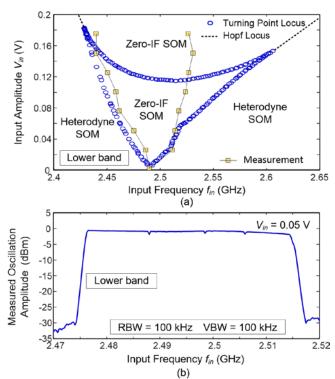

Fig. 18. Operation regions of the double-functionality SOM at the lower band. (a) Bifurcation loci with experimental points superimposed. (b) Experimental trace of the locking band (using a maximum hold), obtained for $P_{in} = -22$ dBm.

B. Conversion gain

One can evaluate the conversion gain of the zero-IF SOM by applying the conversion matrix approach [25], [41] along the closed-synchronization curves. This is done linearizing the HB system about the injection-locked solution obtained for each input frequency ω_{in}, in the presence of an additional input tone at a small offset frequency Ω with respect to ω_{in}. This way, we will be able to estimate the gain when the input signal is composed of a locking tone at ω_{in} (with respect to which the circuit may behave nonlinearly) and an additional small signal with a certain low-power spectrum versus Ω. For this analysis, the value $\Omega/(2\pi) = 1$ MHz will be considered. The gain is defined as the ratio between the output power of at Ω and the available power at $\omega_{in}+\Omega$. The formulation is analogous to the one in (12), though now the HB system is linearized about the periodic solution injection locked to the input tone, instead of the free-running oscillation.

The output signal can be extracted from with the aid of a buffer connected to the resistors R_i, where $i = 1, 2$, in Fig. 4(a). The extraction through the IF filter will be possible provided that the modulation signal has negligible spectral component near DC. This should enable a simplification of the circuit, avoiding additional active devices. Fig. 19(a) compares the simulated and measured gain through the closed synchronization curve obtained for $P_{in} = -16$ dBm when extracting the signal through the IF filter. As gathered from the figure, there is a significant dependence of the gain value on the frequency of the locking tone, and it is possible to obtain gain higher than 5 dB. This value is smaller at the upper band [Fig. 17(b)]. Both with the IF filter and the buffer, the gain increases when approaching the boundaries of the injection-locked band and would tend to infinity for $\Omega \to 0$. Despite the much larger gain values, operation near the band boundaries is not advised due to the small stability margins.
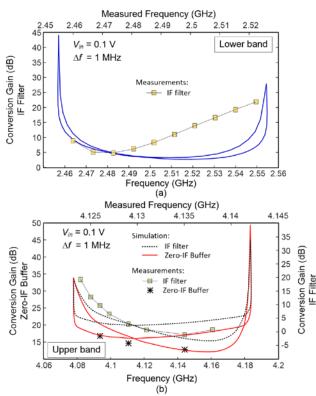
Fig. 19. Variation of conversion gain along the closed synchronization curve obtained for P_{in} = -16 dBm, when considering a small-signal input signal at the offset frequency 1 MHz. The extraction of the output signal through the IF filter is tested. (a) Lower band. (b) Upper band.

C. Behavior under modulated input signals

To optimize the behaviour of a zero-IF SOM with an amplitude-modulated input signal at the carrier frequency ω_{in} it is advisable to trace the synchronized-solution curve versus E_{in}. As shown in Section II.B, this solution curve will be multivalued, so here it is obtained with the same two-stage procedure in (21). The results are shown in Fig. 20 and they present the variation of the oscillation amplitude at the gate node V_{gate} versus E_{in} at the lower and upper operation bands. In each case, three curves have been calculated, at distinct values of input frequency ω_{in}. Note that the "S" shape of the curves was explained in the analytical study of Section II.B. In Fig. 20, for E_{in} values lower that the one corresponding to the turning point T_2, the oscillation is unlocked and mixes with the input signal at ω_{in}, so the circuit behaves in a quasi-periodic regime. The point T_2 is a local-global bifurcation at which the oscillation gets locked when increasing E_{in} [22]. In agreement with the discussions of Section II, the locking takes place for lower E_{in} when reducing the detuning with respect to the free-running frequency (compare Fig. 17 and Fig. 20).
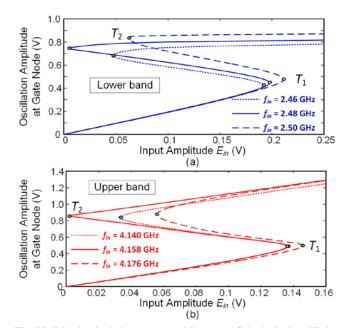

Fig. 20. Injection-locked curves traced in terms of the locked oscillation amplitude at the gate node versus the input amplitude E_{in}. (a) Lower band. (b) Upper band.

Now an AM modulation with a rectangular signal will be considered, as done in [1]. The circuit is analysed with envelope transient, considering a single fundamental frequency, given by that of the input source ω_{in}. In a manner similar to what was done in Section IV.C, an AG is used to initialize the oscillation. The AG frequency ω_{AG}, amplitude V_{AG} and phase shift ϕ with respect to the input source are the ones resulting from the fulfilment of $Y_{AG} = 0$ in the absence of modulations. As in Section IV.C, the AG is connected to the circuit at the initial time only. If the operation conditions are such that the modulated input amplitude goes below the turning point T_2 in Fig. 20, the circuit undergoes an instantaneous unlocking, which may give rise to strong distortion effects. This can be seen in the envelope transient analyses of Fig. 21, where an amplitude modulation with a rectangular waveform of 2 MHz, centred about $E_{in} = 0.07$ V with two different amplitudes, has been considered.

To facilitate the comparison of the amplitude excursion with the static curve E_{in}-V_{gate} in Fig. 20 (providing the oscillation amplitude versus the input amplitude), the two rectangular waveforms are superimposed on this curve in Fig. 21(a). If the lower limit of the rectangular signal is above the turning point T_2 of the static curve for the whole amplitude excursion, there will be no instantaneous unlocking, as in the case of Fig. 21(b). If the lower level is below T_2, an oscillation is observed at the beat frequency, or difference between the input and oscillation frequencies. This is the case of Fig. 17(c). More cycles of the beat frequency will be observed for a lower modulation frequency. The experimental waveforms for the same conditions of (b) and (c) are shown in (d) and (e). Because the input spectrum exhibits negligible content near DC, these signals could be extracted through the IF filter, which has the benefit of suppressing the DC levels. As gathered from Fig. 20, to avoid the instantaneous unlocking, one should increase the carrier power or choose a carrier frequency closer to the free-running one. Note that under an input modulation there will also be dynamic effects due to the non-negligible values of the time derivatives of the state variables, as discussed in Section II. These effects will be

more relevant near the turning point T_2 and can lead to unlocking before reaching this point.

As demonstrated in Section II.B, the zero-IF SOM can also demodulate an FSK signal. The circuit in Fig. 4(a) has been tested for this function, and the simulated results when considering an FSK of 1 Mbps at f_{in} = 4.1 GHz and E_{in} = 0.1 V are shown in Fig 22(a). Due to laboratory equipment limitations, measurements [Fig. 22(b)] have been performed for a frequency modulation (FM) with a square wave of modulation rate of 5 kHz and FM deviation of 5 MHz.
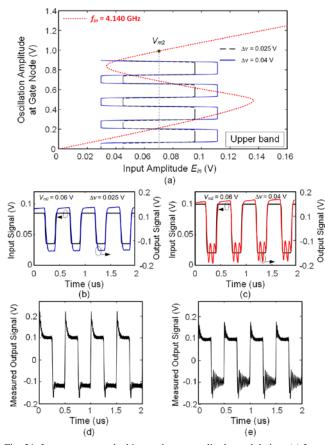

Fig. 21. Instantaneous unlocking under an amplitude modulation. (a) Input-modulation waveforms superimposed on the static curve providing the locked-oscillation amplitude versus the input amplitude (E_{in}-V_{gate}). (b) Input and output waveforms for ΔV = 0.025 V. Correct behaviour. (b) Input and output waveforms for ΔV = 0.04 V. Instantaneous unlocking. (c) Measured waveform under correct operation. (d) Measured waveform exhibiting instantaneous unlocking.
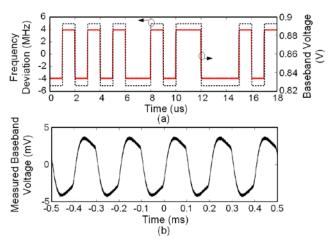

Fig. 22. Operation of the zero-IF SOM as an FSK and FM demodulator. (a) Simulation results as an FSK demodulator. (b) Experimental validation of the FM demodulation capability for a frequency modulation (FM) with a square wave of modulation rate of 5 kHz and FM deviation of 5 MHz.

VI. CONCLUSION

A concurrent dual self-oscillating mixer with double functionality has been presented and investigated in detail. It is based on a concurrent dual-frequency oscillator implemented with a ring-shaped stepped-impedance resonator that exhibits two independent resonances at the frequencies 2.4 GHz and 4.1 GHz with an excellent isolation. The circuit can behave as a concurrent heterodyne mixer and as a zero-IF mixer. The circuit operation has been exhaustively investigated in both linear and nonlinear conditions with respect to the input source. In heterodyne mode, the variation of the conversion gain versus the input power has been analyzed through a contour-intersection method that, in addition to a nonlinear admittance function at the oscillation frequency, requires the extraction and interpolation of a gain function. The input frequency and input power values for operation as a zero-IF SOM have been obtained through a bifurcation detection technique, able to predict the injection-locking bands. The small-signal gain in the presence of the locking tone has been analyzed applying the conversion-matrix approach along the closed injection-locked solution curve. The instantaneous unlocking under a modulated input signal has been investigated and a simple criterion to avoid this undersired phenomenon has been provided.

REFERENCES

[1] P. Burasa, N. G. Constantin and K. Wu , "Zero–IF Self–Oscillating Mixer for High Gbit/s Data–Rate Battery–Free Active uRFID Tag at Millimeter–Wave Frequencies in 65–nm CMOS," *IEEE Trans Microw. Theory Techn.*, vol. 64, no. 4, pp. 1055–1065, 2016.

[2] P. Burasa, B. Mnasri and K. Wu, "Millimeter-Wave CMOS Sourceless Receiver Architecture for 5G-Served Ultra-Low-Power Sensing and Communication Systems," *IEEE Trans Microw. Theory Techn.*, vol. 67, no. 5, pp. 1688-1696, May 2019.

[3] P. Burasa, B. Mnasri and K. Wu, "A Sourceless Low-Power mmW Receiver Architecture Using Self-Oscillating Mixer Array in 65-nm CMOS," 2018 *IEEE Wireless Power Transfer Conf.* (WPTC), Montreal, QC, Canada, 2018, pp. 1-3.

[4] M. Pontón, A. Herrera, A.Suárez, "Analysis and design of a concurrent dual-band self-oscillating mixer," *IEEE MTT-S Int. MIcrow. Symp. Dig.*, Los Angeles, CA, 2020, pp. 1-4.

[5] U. L. Rohde and A. K. Poddar, "Concurrent, reconfigurable, and adaptable oscillators for multi–band multi–mode communication systems," *Proc. 37th Eur. Microw. Conf.*, Oct. 2007, pp. 292–295.

[6] J. S. Schaffner, "Simultaneous oscillations in oscillators", *Trans. of the IRE*, vol.CT–1, no.2, pp.2–8, June 1954.

[7] A. Goel and H. Hashemi, "Concurrent dual-frequency oscillators and phase-lock loops," *IEEE Trans. Microw. Theory Techn.*, vol. 56, no. 8, pp. 1846–1860, Aug. 2008..

[8] F. Ramírez, S. Sancho and A. Suárez, "Oscillation Modes in Multiresonant Oscillator Circuits," *IEEE Trans. Microw. Theory Techn*, vol. 64, no. 12, pp. 4660–4675, Dec. 2016.

[9] M. Sagawa, M. Makimoto, and S. Yamashita, "Geometrical structures and fundamental characteristics of microwave stepped-impedance resonators," *IEEE Trans. Microw. Theory Tech.*, vol. 45, no. 7, pp. 1078–1085, Jul. 1997.

[10] Lung-Hwa Hsieh and Kai Chang, "High-efficiency piezoelectric-transducer-tuned feedback microstrip ring-resonator oscillators operating at high resonant frequencies," *IEEE Trans. Microw. Theory Tech.*, vol. 51, no. 4, pp. 1141-1145, April 2003.

[11] W. Wang, Q. Cao and Y. Zheng, "Bandstop Frequency-Selective Structures Based on Stepped-Impedance Loop Resonators: Design, Analysis, and Measurement," *IEEE Trans. Antennas Propag.* vol. 67, no. 2, pp. 1053-1064, Feb. 2019.

[12] B. Li, Y. Liu, C. Yu and Y. Wu, "A Novel Concurrent Dual–Band Oscillator Based on a Single Ring Resonator," *IEEE Microw. Wireless Comp. Lett.*, vol. 26, no. 8, pp. 607–609, Aug. 2016.

[13] B. Li, Y. Wu, C. Yu and Y. Liu, "Independently Tunable Concurrent Dual-Band VCO Using Square Open-Loop Resonator," *IEEE Access*, vol. 6, pp. 12634-12641, 2018.

[14] B. Li, Y. Liu, C. Yu and Y. Wu, "Independent Control Function for Concurrent Dual-Band VCO," *IEEE Microw. Wireless Compon. Lett.*, vol. 28, no. 3, pp. 230-232, March 2018.

[15] M. Nick and A. Mortazawi, "A very low phase-noise voltage-controlled oscillator at X-band," *IEEE MTT-S Int. Dig.*, Baltimore, MD, USA, Jun. 2011, pp. 1–4.

[16] C. E. Saavedra, B. R. Jackson and S. S. K. Ho, "Self-Oscillating Mixers: A Natural Fit for Active Antennas," *IEEE Microw. Magazine*, vol. 14, no. 6, pp. 40-49, Sept.-Oct. 2013.

[17] M.-R. Tofighi and A. Daryoush, "A 2.5-GHz InGaP/GaAs differential cross-coupled self-oscillating mixer (SOM) IC *IEEE Microw. Wireless Compon. Lett.*, vol. 15, no. 4, pp. 211–213, Apr. 2005.

[18] Elena de Cos, A. Suárez and S. Sancho, "Envelope transient analysis of self-oscillating mixers," *IEEE Trans. Microw. Theory Tech*.,, vol. 52, no. 4, pp. 1090-1100, April 2004,

[19] J. de Cos and A. Suárez, "Efficient Simulation of Solution Curves and Bifurcation Loci in Injection-Locked Oscillators," *IEEE Trans. Microw. Theory Tech*., vol. 63, no. 1, pp. 181-197, Jan. 2015.

[20] S. Hernández, M. Pontón, A. Suárez, "Simulation Method for Complex Multivalued Curves in Injection-Locked Oscillators," *IEEE Trans. Microw. Theory Tech*., vol. 65, no. 11, pp. 4046-4062, Nov. 2017.

[21] J. Guckenheimer, P. J. Holmes, *Nonlinear Oscillations, Dynamical Systems, and Bifurcations of Vector Fields*, Springer, New York 1983.

[22] J. M. T. Thomson, H. B. Stewart, *Nonlinear Dynamics and Chaos*, John Wiley & Sons, 2002.

[23] A. Suárez, *Analysis and Design of Autonomous Microwave Circuits*. Hoboken, NJ: Wiley IEEE Pres, 2009.

[24] R. Quere, E. Ngoya, M. Camiade, A. Suarez, M. Hessane and J. Obregon, "Large signal design of broadband monolithic microwave frequency dividers and phase-locked oscillators," *IEEE Trans. Microw. Theory Tech*., vol. 41, no. 11, pp. 1928-1938, Nov. 1993.

[25] V. Rizzoli and A. Neri, "State of the art and present trends in nonlinear microwave CAD techniques," *IEEE Trans. Microw. Theory Tech*., vol. 36, no. 2, pp. 343-365, Feb. 1988.

[26] A. Suárez, R. Quéré, *Stability Analysis of Nonlinear Microwave Circuits*. Artech House, Norwood (Ma), Jan. 2003.

[27] A. Suárez and F. Ramírez, "Stability and Bifurcation Analysis of Multi–Element Non–Foster Networks," *IEEE Trans. Microw. Theory Tech*., vol. 66, no. 4, pp. 1817–1830, 2018.

[28] E. Ngoya and R. Larchèveque, "Envelop transient analysis: A new method for the transient and steady state analysis of microwave communication circuits and systems," *IEEE MTT-S Int. Microw. Symp. Dig.*, San Francisco, CA, USA, Jun. 1996, pp. 1365–1368.

[29] K. Kurokawa, "Noise in Synchronized Oscillators," *IEEE Trans. Microw. Theory Techn.*, vol. 16, no. 4, pp. 234-240, April 1968.

[30] B. N. Biswas, A. Bhattacharya, P. Lahiri and D. Mondal, "A novel scheme for reception using an active microstrip antenna," *IEEE Trans. Microw. Theory Tech.*, vol. 48, no. 10, pp. 1765-1768, Oct. 2000

[31] E. Main and D. Coffing, "FM demodulation using an injection-locked oscillator," *IEEE MTT-S Int. Dig*, Boston, MA, USA, 2000, pp. 135-138, vol.1

[32] M. Pontón, F. Ramírez, A. Herrera and A. Suarez, "Oscillator Stabilization Through Feedback With Slow Wave Structures," *IEEE Trans. Microw. Theory Techn.*, vol. 68, no. 6, pp. 2358-2373, June 2020.

[33] M. Pontón, A. Herrera and A. Suárez, "Wireless-Coupled Oscillator Systems With an Injection-Locking Signal," *IEEE Trans. Microw. Theory Techn.*, vol. 67, no. 2, pp. 642-658, Feb. 2019.

[34] J. Jugo, J. Portilla, A. Anakabe, A. Suarez, and J. M. Collantes, "Closed loop stability analysis of microwave amplifiers," *Electron. Lett*., vol. 37, no. 4, pp. 226–228, Feb. 2001.

[35] J. M. Collantes, I. Lizarraga, A. Anakabe and J. Jugo, "Stability verification of microwave circuits through Floquet multiplier analysis," *IEEE Asia-Pacific Conf. Circuits and Systems*, 2004, Tainan, pp. 997-1000 vol.2,.

[36] N. Ayllon, A. Anakabe, J. M. Collantes, G. Soubercaze-Pun and S. Forestier, "Sensitivity Enhancement in Pole-Zero Identification Based Stability Analysis of Microwave Circuits," *Workshop Integ. Nonlin. Microw. Millimetre-Wave Circuits*, Malaga, 2008, pp. 75-78.

[37] A. Anakabe, J. M. Collantes, J. Portilla, et al. "Analysis and elimination of parametric oscillations in monolithic power amplifiers," *IEEE MTT-S Int. Dig*., Seattle, WA, Jun. 2002, pp. 2181–2184.

[38] C. Barquinero, A. Suarez, A. Herrera and J. L. Garcia, "Complete Stability Analysis of Multifunction MMIC Circuits," *IEEE Trans. Microw. Theory Techn*, vol. 55, no. 10, pp. 2024-2033, Oct. 2007.

[39] V. Rizzoli, A. Lipparini, "General stability analysis of periodic steady-state regimes in nonlinear microwave circuits," *IEEE Trans. Microw. Theory Techn*., vol. 33, no. 1, pp. 30 – 37, Jan. 1985.

[40] A. Platzker, W. Struble and K. T. Hetzler, "Instabilities diagnosis and the role of K in microwave circuits," *IEEE MTT-S Int. Dig*., Atlanta, GA, USA, 1993, pp. 1185-1188 vol.3.

[41] J. M. Paillot, J. C. Nallatamby, M. Hessane, R. Quéré, M. Prigent and J. Rousset, "A general program for steady state, stability, and FM noise analysis of microwave oscillators," *IEEE MTT-S Int. Dig*., 1990, Dallas, Tx, May, 1990.pp. 1287–1290.

[42] S. ver Hoeye, L. Zurdo and A. Suarez, "New nonlinear design tools for self-oscillating mixers," *IEEE Microw. Wireless Compon. Lett.*, vol. 11, no. 8, pp. 337-339, Aug. 2001

[43] F. Ramirez, M. Ponton, S. Sancho and A. Suarez, "Phase-Noise Analysis of Injection-Locked Oscillators and Analog Frequency Dividers," *IEEE Trans. Microw. Theory Techn,*, vol. 56, no. 2, pp. 393-407, Feb. 2008.

[44] K. Kurokawa, "Some basic characteristics of broadband negative resistance oscillators," Bell Syst. Tech. J., vol. 48, pp. 1937–1955,Jul./Aug. 1969.

[45] V. Rizzoli, F. Mastri and D. Masotti, "General noise analysis of nonlinear microwave circuits by the piecewise harmonic balance technique," *IEEE Trans. Microw. Theory Techn,*, vol. 42, no. 5, pp. 807–819, May, 1994.

Mabel Pontón (S'08–M'11) was born in Santander, Spain. She received the bachelor's degree in Telecommunication Engineering, master's degree in Information Technologies and Wireless Communications Systems, and Ph.D. degree from the University of Cantabria, Santander, in 2004, 2008, and 2010, respectively. In 2006, she joined the Communications Engineering Department, University of Cantabria.

From 2011 to 2013, she was with the Group of Electronic Design and Applications, Georgia Institute of Technology, Atlanta, GA, USA, as a Post-Doctoral Research Fellow.

Her current research interests include the nonlinear analysis and simulation of radiofrequency and microwave circuits, with an emphasis on phase-noise, stability, and bifurcation analysis of complex oscillator topologies.

Amparo Herrera was born in Asturias (Spain) in 1963. She received the degree in Electronic Physics from the University of Cantabria (Spain) in June 1987, and the Ph.D degree from the same University in June 1995. In 1987 she joined the CIDA (Centro de Investigación y Desarrollo de la Armada) the Research and Development Spanish Army Centre, working on developing a RF&Microwave laboratory up to 1990 when she joined the Electronics Department of the University of Cantabria, working on MMIC design. From 1992 to 1995, she collaborated with the Laboratory Philips Microwave Limeil (actually OMMIC), as result of this collaboration she presents her thesis receiving the Ph.D. degree in Electronics from the University of Cantabria in June 1995 in this work she had designed a high efficiency power amplifier for DECT and DCS applications a work for the Philips Microwave Limeill foundry (now called OMMIC). From 1995 she has been an associate professor at the University of Cantabria, and a member of its Communications Engineering Department. Her areas of interest include the MMIC and Hybrid design of microwave circuits and, specially, the power and low noise amplifier design and characterization. She has taken part as Main researcher in a big number of Spanish and European projects both of the III, IV, V and VI Frameworks and Spanish National R&D Plan. Also she has participated in a number of industrial projects with European and Spanish industries. Currently she is working in the design and development of MMIC devices on Si-Ge, GaN PHEMT technologies.

Almudena Suárez (M'96–SM'01–F'12) was born in Santander, Spain. She received the Licentiate degree in Electronic Physics and the Ph.D. degree from the University of Cantabria, Santander, Spain, in 1987 and 1992, respectively, and the Ph.D. degree in Electronics from the University of Limoges, Limoges, France, in 1993. She is currently a full professor at University of Cantabria (Spain) and head of the research group Microwave Engineering and Radiocommunication Systems. She is a Fellow member of the IEEE (Institute of Electrical and Electronic Engineers, New Jersey, USA). She was

also an IEEE Distinguished Microwave Lecturer during the period 2006-2008. She has authored the book *Analysis and design of autonomous microwave circuits* (IEEE-Wiley, 2009) and co-authored the book *Stability analysis of nonlinear microwave circuit'* (Artech House, 2003).

Prof. Suárez is a member of the technical committees of IEEE International Microwave Symposium (IEEE MTT-S) and the European Microwave Week. She is a member of the Board of Directors of European Microwave Association. She is an associate editor of IEEE Microwave Magazine. She was the coordinator of the Communications and Electronic Technology Area for the Spanish National Evaluation and Foresight Agency (ANEP) between 2009 and 2013. She was the chair of the 2014 and 2015 editions of IEEE Topical Conference on RF/Microwave Power Amplifiers (PAWR), in Newport Beach and San Diego. She was the General TPC Chair of European Microwave Wekk 2018. Prof. Suárez was the Editor-in-Chief of the International Journal of Microwave and Wireless Technologies from Cambridge University Press journals from 2013 to 2018 and is currently an Associate Editor for IEEE Microwave Magazine and the IEEE Transactions on Microwave Theory and Techniques.